NJC

ROYAL SOCIETY OF CHEMISTRY

PAPER

View Article Online
View Journal | View Issue



Cite this: *New J. Chem.*, 2024, **48**, 8093

# Adsorption of gases on $B_{12}N_{12}$ and $Al_{12}N_{12}$ nanocages†

Remya Geetha Sadasivan Nair, * Arun Kumar Narayanan Nair * and Shuyu Sun*

Density functional theory (DFT) was used to investigate the adsorption of twenty-four gases ($SiH_4$, $H_2$, $Cl_2$, $F_2$, $CF_4$, $CH_4$, $CF_2Cl_2$, $N_2$, $CHF_3$, OCS, $N_2O$, $AsH_3$, $CH_3Cl$, $COCl_2$, $C_2H_2$, $C_2H_4$, $H_2Se$, $H_2S$, $PH_3$, $COF_2$, $CH_3F$, HCHO, $(CH_3)_2O$, and $CH_3NH_2$) on $B_{12}N_{12}$ and $Al_{12}N_{12}$ nanocages. Most of the studied gases are weakly (strongly) adsorbed on the $B_{12}N_{12}$ ($Al_{12}N_{12}$) nanocage. However, $AsH_3$, $H_2Se$, $H_2S$, $PH_3$, $CH_3F$, HCHO, $(CH_3)_2O$, and $CH_3NH_2$ are strongly adsorbed on the $B_{12}N_{12}$ nanocage and $H_2$, $F_2$, $CF_4$, $CH_4$, and $CF_2Cl_2$ are weakly adsorbed on the $Al_{12}N_{12}$ nanocage. The most negative-valued molecular electrostatic potential (MESP) minimum ($V_{min}$) corresponds to the electron-rich region (*e.g.*, lone pair and π-bond) in the molecule. An important observation is that the adsorption energies of the gases on the $B_{12}N_{12}$ and $Al_{12}N_{12}$ nanocages are well correlated with the MESP $V_{min}$ values of the gases. Substantial changes are found in the DFT reactivity indices like chemical potential and hardness of the $B_{12}N_{12}$ and $Al_{12}N_{12}$ nanocages, mainly due to the strong gas adsorption. The quantum theory of atoms in molecules analysis suggests the covalent nature of interactions only in the $AsH_3/B_{12}N_{12}$, $H_2Se/B_{12}N_{12}$, $H_2S/B_{12}N_{12}$, and $PH_3/B_{12}N_{12}$ systems.

Received 12th December 2023,
Accepted 29th March 2024

DOI: 10.1039/d3nj05703h

rsc.li/njc



## 1. Introduction

Air pollution due to rapid urbanization and economic developments is a major environmental concern. Methane ($CH_4$) and nitrous oxide ($N_2O$) are the most important anthropogenic contributors to the greenhouse effect after carbon dioxide ($CO_2$).[1,2] Enteric fermentation and the oil and gas industry have been identified as the two main sources of anthropogenic $CH_4$. The use of nitrogen fertilizers is identified as an important source of nitrous oxide ($N_2O$) emissions. Hydrogen sulfide ($H_2S$) is a highly toxic gas released from sewage treatment processes, fuel burning, and petroleum extraction.[3] Carbonyl sulfide (OCS) is released from the burning of biomass and fossil fuel, as well as petrochemical and gasification processes.[4] Halomethanes are found both in marine environments and those of man-made origin, and some of them are widespread and hazardous.[5,6] For example, the ultraviolet photolysis of refrigerants such as dichlorodifluoromethane ($CF_2Cl_2$) can damage the stratospheric ozone layer. Silane ($SiH_4$) finds applications in the photovoltaic and semiconductor industries.[7] Hydrogen selenide ($H_2Se$) is used in the preparation of materials for battery applications.[8] Chlorine ($Cl_2$) can be used for the sterilization of drinking water.[9] Fluorine ($F_2$) plays a key role in the pharmaceutical industry.[10] The pnictogen hydride gases phosphine ($PH_3$)[11] and arsine ($AsH_3$)[12] are used as a fumigant and in the semiconductor industry, respectively. Phosgene ($COCl_2$) is of historical interest (chemical weapon in World War I) and currently used in the manufacture of polyurethanes, polycarbonates, dyestuff, pharmaceuticals, *etc.*[13] The usage of carbonyl fluoride ($COF_2$) as a cleaning gas could reduce the greenhouse gas emissions from the semiconductor industry.[14] Formaldehyde (HCHO) is mainly used to synthesize resins.[15] Dimethyl ether ($(CH_3)_2O$) can be used as an aerosol propellant and as an alternative to diesel fuel.[16] Methylamine ($CH_3NH_2$) is used for fabricating perovskite solar cells.[17] However, these gases could cause severe health and safety concerns. Hydrogen ($H_2$) storage is a key issue in developing materials which could be utilized for fuel cell technology.[18] Nitrogen ($N_2$) is often used in modeling the adsorption process.[19] There are growing interests in gas capture and storage necessitated by concerns arising from the demand to mitigate air pollution. Materials like metal–organic framework, zeolite, graphene, fullerene, carbon nanotube, polymer, clay, cyclo[*n*]carbon, *etc.* exhibit promising potential for applications in gas capture and storage.[20–27]

There have been density functional theory (DFT) studies of the gas-adsorption on nanoparticles and nanosheets. Abbasi *et al.* found that the adsorption of $NO_2$, $CH_2O$ and $H_2S$ molecules on the N-doped $TiO_2$ anatase nanoparticles is energetically more favorable than the adsorption on the pristine ones.[28–30] The adsorption behaviors of $SO_x$ molecules showed

*Physical Science and Engineering Division (PSE), Computational Transport Phenomena Laboratory, King Abdullah University of Science and Technology (KAUST), Thuwal 23955-6900, Saudi Arabia. E-mail: remya.nair@kaust.edu.sa, arun.narayanannair@kaust.edu.sa, shuyu.sun@kaust.edu.sa*

† Electronic supplementary information (ESI) available: Additional details of DFT analysis. See DOI: https://doi.org/10.1039/d3nj05703h

an improved adsorption ability for N-doped ZnO nanoparticles over undoped nanoparticles.[31] The interaction of $O_3$ and $NO_2$ with the N-doped $TiO_2$/ZnO nanocomposite was stronger than with the pristine one.[32] The noble metal (Rh, Pt, Pd) decorated N-doped graphene may potentially be used as sensors for biogas detection.[33] The B-doped stanene may be a good candidate for gas sensing.[34,35] It was found that the $O_3$, $SO_2$, and $SO_3$ molecules weakly interact with the $MoS_2$ monolayer.[36] The adsorption of CO and NO molecules on the doped $MoS_2$ monolayers was more favorable in energy than that on the pristine monolayers.[37]

The gas-adsorption on fullerene-like $B_{12}N_{12}$ and $Al_{12}N_{12}$ nanocages has attracted a lot of interest in recent years.[27,38–51] The synthesis of the fullerene-like $B_{12}N_{12}$ nanocage clusters has been reported.[52] There have been reports of the synthesis of AlN nanotube and nanocone.[53,54] The $Al_{12}N_{12}$ nanocage has been computed to be the most stable of the $Al_nN_n$ ($n$ = 2–41) nanocages.[55] The DFT studies showed that the adsorption of $CH_4$ has no significant effect on the electronic properties of the $B_{12}N_{12}$ nanocage.[38] $H_2S$ showed a weak physisorption on the $B_{12}N_{12}$ nanocage.[39] The formaldehyde adsorption induced considerable variation in the electronic properties of the $B_{12}N_{12}$ nanocage.[40] The adsorption of $N_2$ and $F_2$ showed negligible changes on the electronic and structural properties of the $B_{12}N_{12}$ nanocage.[41] Higher values of adsorption energy were obtained for $CH_3F$ than for $CH_3Cl$ on the $B_{12}N_{12}$ nanocage.[42] $NH_3$ molecule was adsorbed on the $B_{12}N_{12}$ nanocage with considerable adsorption energy, while the $PH_3$ and $AsH_3$ molecules were relatively weakly adsorbed.[43] DFT studies showed that $CH_3Cl$ and $CH_3F$ strongly interact with the $Al_{12}N_{12}$ nanocage.[44] It was found that $H_2S$ and OCS strongly interact with the $Al_{12}N_{12}$ nanocage.[45] Acetylene and ethylene interact preferably with an Al atom rather than N atom of the $Al_{12}N_{12}$ nanocage.[46] A very weak adsorption of $H_2$ on the $B_{12}N_{12}$ and $Al_{12}N_{12}$ nanocages has been reported.[47–49] It was found that dimethyl ether chemisorbed on the $B_{12}N_{12}$ and $Al_{12}N_{12}$ nanocages.[50] The adsorption of phosgene molecules on the $B_{12}N_{12}$ ($Al_{12}N_{12}$) nanocage proceeds by way of physisorption (chemisorption).[51] We recently investigated the adsorption process of NO, $CO_2$, CO, and $NH_3$ on the $B_{12}N_{12}$ and $Al_{12}N_{12}$ nanocages using DFT calculations.[27] It was found that, for example, $NH_3$ chemisorbed on the $B_{12}N_{12}$ and $Al_{12}N_{12}$ nanocages.[27] However, adsorption of gases like $SiH_4$ on the $B_{12}N_{12}$ and $Al_{12}N_{12}$ nanocages has yet to be studied.

In this study, we perform DFT calculations to understand the adsorption behavior of $SiH_4$, $H_2$, $Cl_2$, $F_2$, $CF_4$, $CH_4$, $CF_2Cl_2$, $N_2$, $CHF_3$, OCS, $N_2O$, $AsH_3$, $CH_3Cl$, $COCl_2$, $C_2H_2$, $C_2H_4$, $H_2Se$, $H_2S$, $PH_3$, $COF_2$, $CH_3F$, HCHO, $(CH_3)_2O$, and $CH_3NH_2$ on the $B_{12}N_{12}$ and $Al_{12}N_{12}$ nanocages. Most of the studied gases are weakly (strongly) adsorbed on the $B_{12}N_{12}$ ($Al_{12}N_{12}$) nanocage. The most negative-valued molecular electrostatic potential (MESP) minimum ($V_{min}$) corresponds to the electron-rich region (*e.g.*, lone pair and π-bond) in the molecule.[56–58] An important observation is that the adsorption energies of the gases on the $B_{12}N_{12}$ and $Al_{12}N_{12}$ nanocages are well correlated with the MESP $V_{min}$ values of the gases. Our results are expected to contribute to the exploration and development of promising adsorbents for gas capture and sequestration.

## 2. Computational details and calculations

We recently studied the adsorption of NO, $CO_2$, CO, and $NH_3$ on $B_{12}N_{12}$ and $Al_{12}N_{12}$ nanocages using DFT calculations.[27] Here we study the adsorption of an additional 24 gases ($SiH_4$, $H_2$, $Cl_2$, $F_2$, $CF_4$, $CH_4$, $CF_2Cl_2$, $N_2$, $CHF_3$, OCS, $N_2O$, $AsH_3$, $CH_3Cl$, $COCl_2$, $C_2H_2$, $C_2H_4$, $H_2Se$, $H_2S$, $PH_3$, $COF_2$, $CH_3F$, HCHO, $(CH_3)_2O$, and $CH_3NH_2$) on $B_{12}N_{12}$ and $Al_{12}N_{12}$ nanocages using DFT calculations. All the DFT calculations were performed with the Gaussian 16 code.[59] All structures were optimized at the M062X/6-311G(d,p) level.[60] The harmonic frequencies (all positive) were computed to confirm the minimal nature of the optimized structures. The MESP topographical analysis of molecules were

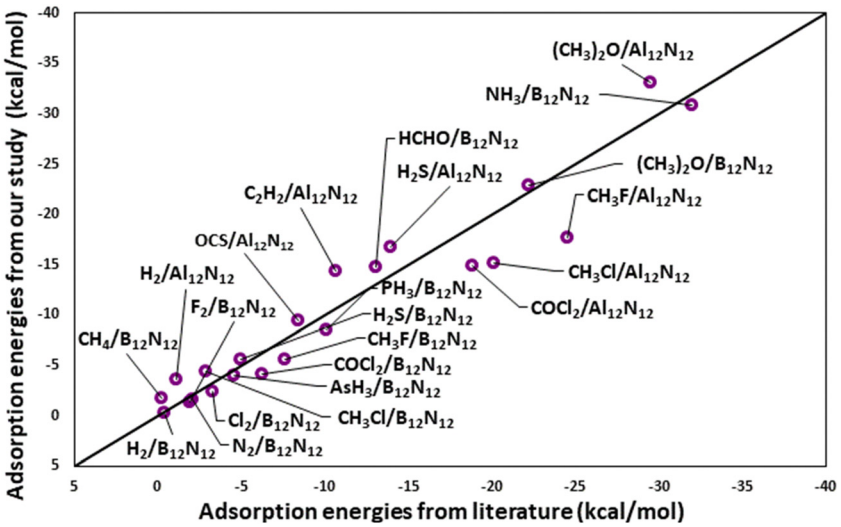


Fig. 1 Comparison of our results for adsorption energies with literature values.[38–51]

 

performed at the M062X/6-311G(d,p) level. The MESP, $V(\mathbf{r})$, is expressed as[56–58]

$$V(\mathbf{r}) = \sum_{A=1}^{N} \frac{Z_A}{|\mathbf{r} - \mathbf{R}_A|} - \int \frac{\rho(\mathbf{r}')}{|\mathbf{r} - \mathbf{r}'|} \mathrm{d}^3\mathbf{r}' \quad (1)$$

where $Z_A$ and $\rho(\mathbf{r})$ represent charge on nucleus $A$ located at $\mathbf{R}_A$ and electronic charge density, respectively. The first and second terms in eqn (1) stand for the nuclear and electronic contributions, respectively. The sign of $V(\mathbf{r})$ is positive when the first term in eqn (1) is dominant and negative when the second term in eqn (1) is dominant.

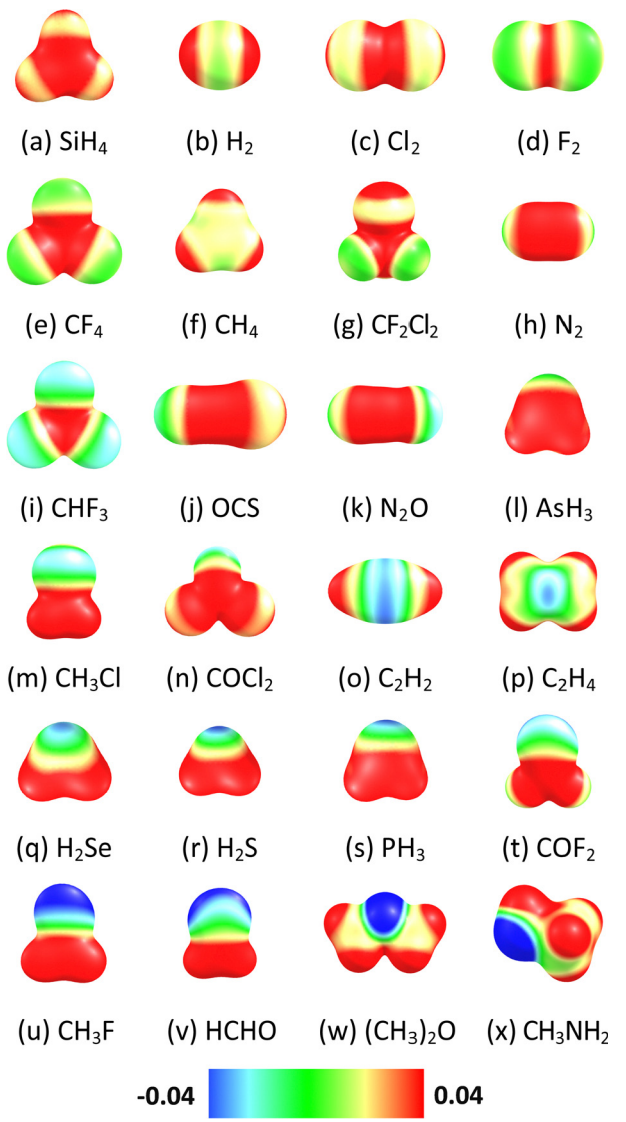


Fig. 2 MESP mapped onto the 0.01 a.u. electron density isosurface of (a) $SiH_4$, (b) $H_2$, (c) $Cl_2$, (d) $F_2$, (e) $CF_4$, (f) $CH_4$, (g) $CF_2Cl_2$, (h) $N_2$, (i) $CHF_3$, (j) OCS, (k) $N_2O$, (l) $AsH_3$,(m) $CH_3Cl$, (n) $COCl_2$, (o) $C_2H_2$, (p) $C_2H_4$, (q) $H_2Se$, (r) $H_2S$, (s) $PH_3$, (t) $COF_2$, (u) $CH_3F$, (v) HCHO, (w) $(CH_3)_2O$, and (x) $CH_3NH_2$. Color code: blue −0.04 a.u. to red 0.04 a.u. Blue represents the most electron-rich region and red the most electron-poor region.

The DFT reactivity indices are given by[61–66]

$$\text{Electronic chemical potential, } \mu = \frac{E_{\mathrm{LUMO}} + E_{\mathrm{HOMO}}}{2} \quad (2)$$

$$\text{Chemical hardness, } \eta = \frac{E_{\mathrm{LUMO}} - E_{\mathrm{HOMO}}}{2} \quad (3)$$

$$\text{Global softness, } S = \frac{1}{2\eta} \quad (4)$$

$$\text{Global electrophilicity, } \omega = \frac{\mu^2}{2\eta} \quad (5)$$

where $E_{\mathrm{HOMO}}$ and $E_{\mathrm{LUMO}}$ denote the energy of the highest occupied molecular orbital (HOMO) and the lowest unoccupied molecular orbital (LUMO), respectively. These DFT reactivity indices may give insight into the chemical reactivities.

The adsorption energy ($E_{\mathrm{ads}}$) is given by

$$E_{\mathrm{ads}} = E_{\mathrm{gas/nanocage}} - (E_{\mathrm{nanocage}} + E_{\mathrm{gas}}) \quad (6)$$

where $E_{\mathrm{gas/nanocage}}$, $E_{\mathrm{nanocage}}$, and $E_{\mathrm{gas}}$ represent the energy of gas-adsorbed nanocage, nanocage (*e.g.*, $B_{12}N_{12}$), and gas (*e.g.*, $SiH_4$), respectively.

The adsorption free energy ($G_{\mathrm{ads}}$) is given by

$$G_{\mathrm{ads}} = G_{\mathrm{gas/nanocage}} - (G_{\mathrm{nanocage}} + G_{\mathrm{gas}}) \quad (7)$$

where $G_{\mathrm{gas/nanocage}}$, $G_{\mathrm{nanocage}}$, and $G_{\mathrm{gas}}$ represent the free energy of gas-adsorbed nanocage, nanocage, and gas respectively. The adsorption energies and free energies were corrected for the basis set superposition errors with the counterpoise method.[67] It may be noted that our $E_{\mathrm{ads}}$ values are consistent with earlier works[38–51] (Fig. 1).

Furthermore, Bader's quantum theory of atoms in molecules (QTAIM) analysis[68] at the M062X/6-311G(d,p) level was performed using Multiwfn software.[69] The covalent and noncovalent bonding scenario can be analyzed based on the value of $\rho$ and its Laplacian ($\nabla^2\rho$) at the bond critical point. Usually, for the covalent interaction, $\rho$ is relatively high and $\nabla^2\rho < 0$, while for the non-covalent interaction (van der Waals, ionic, *etc.*), $\rho$ is relatively low and $\nabla^2\rho > 0$.[70,71] The electron localization function (ELF)[72] and localized orbital locator (LOL)[73] were calculated

Table 1 MESP $V_{\mathrm{min\text{-}X}}$ for adsorbate gases. Values in kcal mol$^{-1}$

| Adsorbate | $V_{\mathrm{min\text{-}X}}$ | Adsorbate | $V_{\mathrm{min\text{-}X}}$ |
|---|---|---|---|
| $SiH_4$ | −0.94 | $AsH_3$ | −15.88 |
| $H_2$ | −2.64 | $CH_3Cl$ | −17.07 |
| $Cl_2$ | −2.76 | $COCl_2$ | −20.65 |
| $F_2$ | −2.76 | $C_2H_2$ | −21.15 |
| $CF_4$ | −2.95 | $C_2H_4$ | −21.27 |
| $CH_4$ | −3.07 | $H_2Se$ | −21.77 |
| $CF_2Cl_2$ | −3.89 | $H_2S$ | −23.78 |
| NO[a] | −8.97 | $PH_3$ | −23.91 |
| $N_2$ | −11.92 | $COF_2$ | −24.85 |
| $CHF_3$ | −12.86 | $CH_3F$ | −31.31 |
| OCS | −14.12 | HCHO | −41.92 |
| $CO_2$[a] | −14.87 | $(CH_3)_2O$ | −52.02 |
| $N_2O$ | −15.19 | $NH_3$[a] | −73.23 |
| CO[a] | −15.88 | $CH_3NH_2$ | −75.80 |

[a] Taken from ref. 27.

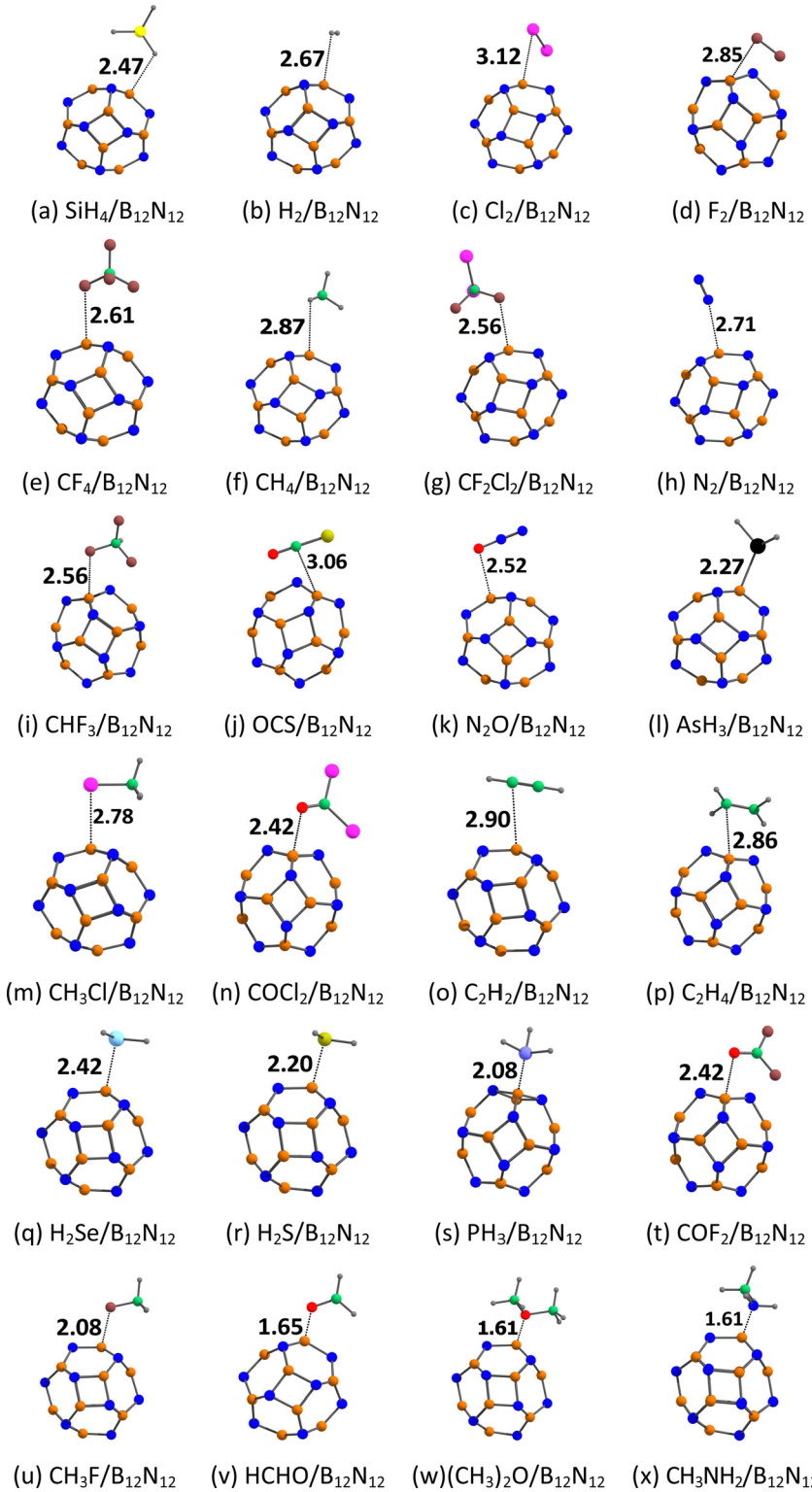


Fig. 3 Optimized structures of gases (a) $SiH_4$, (b) $H_2$, (c) $Cl_2$, (d) $F_2$, (e) $CF_4$, (f) $CH_4$, (g) $CF_2Cl_2$, (h) $N_2$, (i) $CHF_3$, (j) OCS, (k) $N_2O$, (l) $AsH_3$, (m) $CH_3Cl$, (n) $COCl_2$, (o) $C_2H_2$, (p) $C_2H_4$, (q) $H_2Se$, (r) $H_2S$, (s) $PH_3$, (t) $COF_2$, (u) $CH_3F$, (v) HCHO, (w) $(CH_3)_2O$, and (x) $CH_3NH_2$ adsorbed on $B_{12}N_{12}$. The adsorption distances are given in Å. Color code: green-C, orange-B, blue-N, yellow-Si, gray-H, pink-Cl, brown-F, red-O, cyan-Se, yellowish green-S, black-As, violet-P.

using the Multiwfn program.[69] The relatively high values of ELF and LOL are indicative of covalent interactions. The non-covalent interaction (NCI) analysis[74,75] was performed using the Multiwfn program[69] and the results were visualized with the Gnuplot[76] and visual molecular dynamics (VMD) software.[77]

 

Table 2 Adsorption distance, $E_{ads}$, $G_{ads}$, MESP $V_{min}$, and $\Delta V_{min}$ for the gas-adsorbed $B_{12}N_{12}$ nanocage. $d_{ads}$ is given in Å, other values are given in kcal mol$^{-1}$

| Adsorbate | $d_{ads}$ | $E_{ads}$ | $G_{ads}$ | $V_{min\text{-}C'}$ | $\Delta V_{min\text{-}C}$ |
|---|---|---|---|---|---|
| $SiH_4$ | 2.47 | −2.47 | 5.86 | −21.77 | −1.00 |
| $H_2$ | 2.67 | −0.83 | 3.94 | −21.34 | −0.56 |
| $Cl_2$ | 3.12 | −2.36 | 4.84 | −21.40 | −0.63 |
| $F_2$ | 2.85 | −1.34 | 5.65 | −21.59 | −0.82 |
| $CF_4$ | 2.61 | −2.08 | 6.60 | −21.90 | −1.13 |
| $CH_4$ | 2.87 | −1.70 | 3.21 | −21.27 | −0.50 |
| $CF_2Cl_2$ | 2.56 | −2.20 | 7.32 | −22.84 | −2.07 |
| NO[a] | 2.54 | −2.77 | 3.46 | −22.90 | −2.13 |
| $N_2$ | 2.71 | −1.60 | 3.27 | −22.21 | −1.44 |
| $CHF_3$ | 2.56 | −3.57 | 5.74 | −24.47 | −3.70 |
| OCS | 3.06 | −2.65 | 4.77 | −23.85 | −3.07 |
| $CO_2$[a] | 2.66 | −2.95 | 3.51 | −22.53 | −1.76 |
| $N_2O$ | 2.52 | −3.69 | 3.88 | −24.10 | −3.33 |
| CO[a] | 1.79 | −1.65 | 7.64 | −27.92 | −7.15 |
| $AsH_3$ | 2.27 | −4.05 | 6.27 | −30.94 | −10.17 |
| $CH_3Cl$ | 2.78 | −4.45 | 4.21 | −25.04 | −4.27 |
| $COCl_2$ | 2.42 | −4.11 | 7.00 | −26.17 | −5.40 |
| $C_2H_2$ | 2.90 | −3.54 | 1.64 | −24.85 | −4.08 |
| $C_2H_4$ | 2.86 | −3.87 | 4.04 | −23.22 | −2.45 |
| $H_2Se$ | 2.42 | −4.44 | 3.87 | −28.68 | −7.91 |
| $H_2S$ | 2.20 | −5.64 | 4.45 | −29.81 | −9.04 |
| $PH_3$ | 2.08 | −8.49 | 2.38 | −32.82 | −12.05 |
| $COF_2$ | 2.42 | −3.91 | 5.35 | −26.42 | −5.65 |
| $CH_3F$ | 2.08 | −5.64 | 3.83 | −29.87 | −9.10 |
| HCHO | 1.65 | −14.76 | −2.16 | −33.63 | −12.86 |
| $(CH_3)_2O$ | 1.61 | −22.86 | −9.57 | −34.20 | −13.43 |
| $NH_3$[a] | 1.62 | −30.82 | −18.62 | −34.89 | −14.12 |
| $CH_3NH_2$ | 1.61 | −36.84 | −23.22 | −35.27 | −14.50 |

[a] Taken from ref. 27.

# 3. Results and discussion

## 3.1. MESP

The MESP maps of the gas molecules are given in Fig. 2. A visual check of the MESP maps shows the presence of a blue region (most electron-rich region) in, for example, the formaldehyde, dimethyl ether, and methylamine molecules. The blue region is situated close to the O atoms of the formaldehyde and dimethyl ether molecules, and the N atom of the methylamine molecule. The MESP $V_{min}$ values of the gas molecules (represented as $V_{min\text{-}X}$) are given in Table 1. The locations of the MESP $V_{min}$ for a few representative cases are given in Fig. S1 (ESI†). Here these $V_{min\text{-}X}$ values are in the range of −0.94 ($SiH_4$) to −75.80 kcal mol$^{-1}$ ($CH_3NH_2$). The MESP $V_{min}$ values of the diatomic gases follow the order: $H_2$ < $Cl_2$ < $F_2$ < NO < $N_2$ < CO. The MESP $V_{min}$ values of the triatomic molecules follow the order: OCS < $CO_2$ < $N_2O$ < $H_2Se$ < $H_2S$. The MESP $V_{min}$ value of silane is lower than that of methane (−3.07 kcal mol$^{-1}$). The MESP $V_{min}$ values of the hydrocarbon gases follow the order: methane < acetylene < ethylene. The MESP $V_{min}$ values of the halomethanes follow the order: $CF_4$ < $CF_2Cl_2$ < $CHF_3$ < $CH_3Cl$ < $CH_3F$. The MESP $V_{min}$ values of formaldehyde and its halogenated derivatives follow the order: phosgene < carbonyl fluoride < formaldehyde. The MESP $V_{min}$ value of dimethyl ether (−52.02 kcal mol$^{-1}$) is lower than that of both ammonia (−73.23 kcal mol$^{-1}$) and methylamine. The MESP $V_{min}$ values of the pnictogen hydrides and methylamine follow the order arsine < phosphine < ammonia < methylamine.

Both of the $B_{12}N_{12}$ and $Al_{12}N_{12}$ nanocages consist of 6 tetragonal and 8 hexagonal rings[27,78] (Fig. S2, ESI†). These nanocages have two distinct B–N or Al–N bonds. Here, the two hexagonal rings share the shorter B–N (1.44 Å) or Al–N bond (1.78 Å), and the tetragonal and the hexagonal rings share the longer B–N (1.48 Å) or Al–N bond (1.85 Å). A visual check of the MESP maps shows that the blue regions (most electron-rich regions) are situated close to the N atoms of the $B_{12}N_{12}$ and $Al_{12}N_{12}$ nanocages (see Fig. S2, ESI†). It may be noted that the MESP $V_{min}$ values of $B_{12}N_{12}$ and $Al_{12}N_{12}$ (represented as $V_{min\text{-}C}$) are −20.77 and −49.07 kcal mol$^{-1}$ respectively.[27]

## 3.2. Adsorption of gases on $B_{12}N_{12}$

The optimized structures of the gases adsorbed on the $B_{12}N_{12}$ nanocage are given in Fig. 3. The studied gases are preferably bound to the B atom rather than the N atom of the $B_{12}N_{12}$ nanocage. Notably, the F atom of the $CF_2Cl_2$, the C atom of the

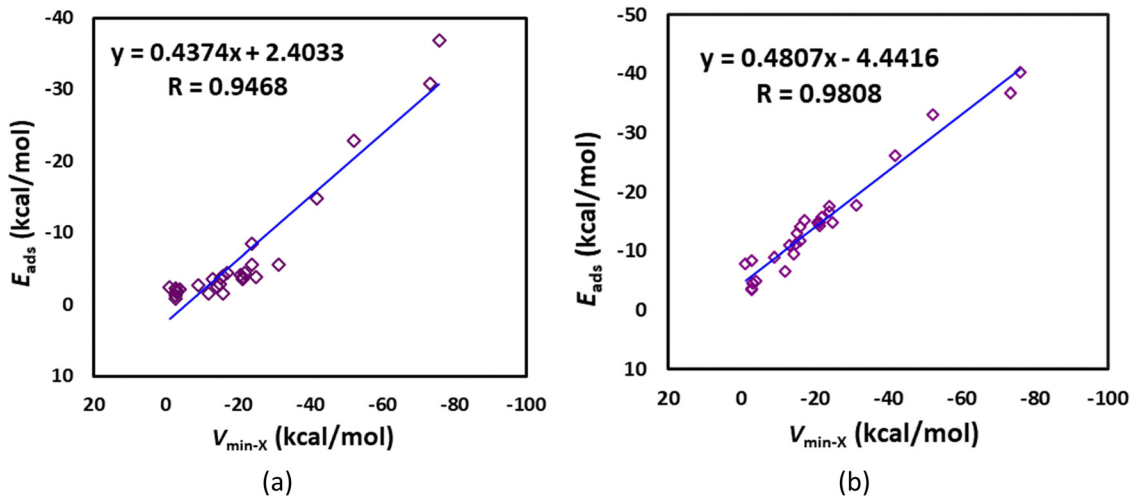


Fig. 4 Correlation between $V_{min\text{-}X}$ and $E_{ads}$ for gas-adsorbed (a) $B_{12}N_{12}$ and (b) $Al_{12}N_{12}$ nanocages.

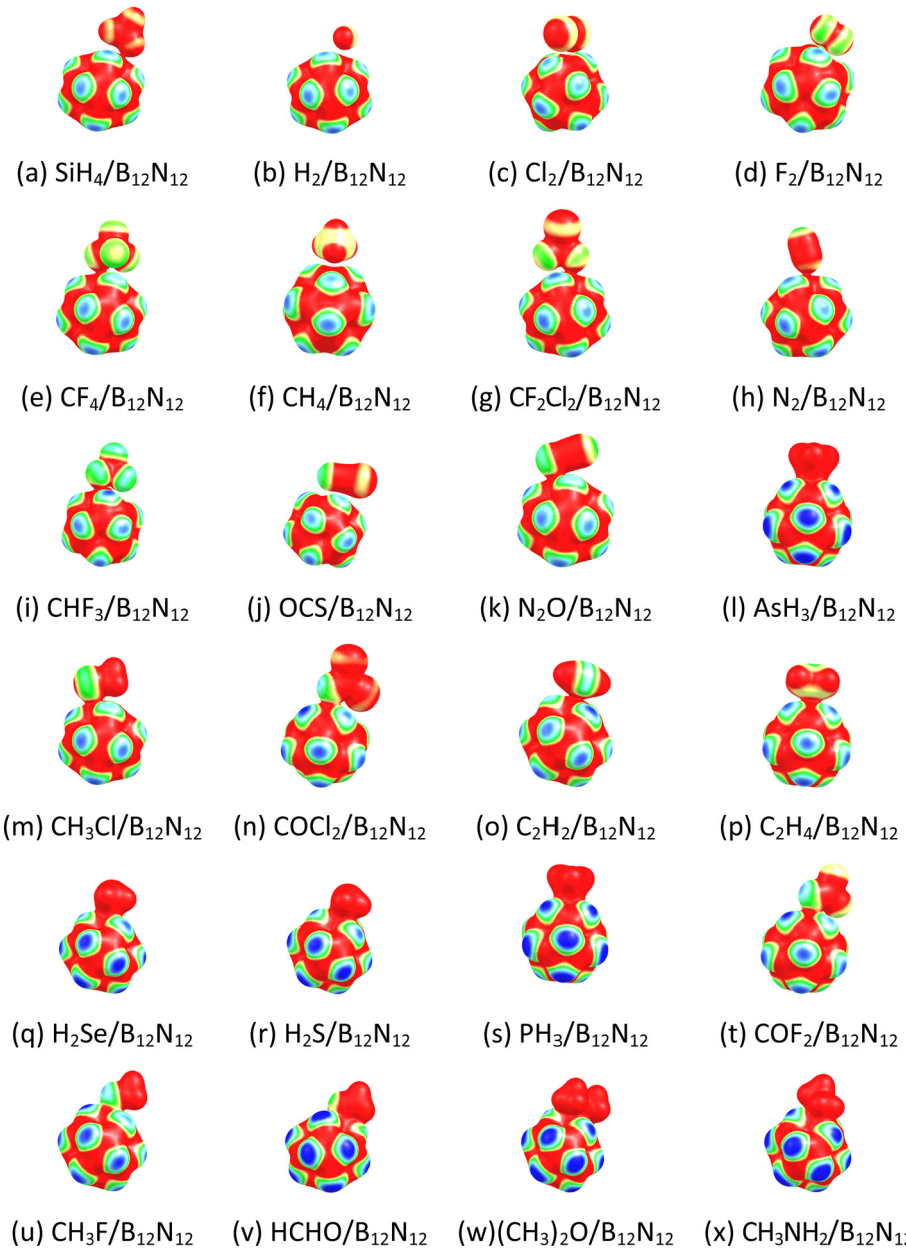


Fig. 5 MESP mapped onto 0.01 a.u. electron density isosurface of gases (a) $SiH_4$, (b) $H_2$, (c) $Cl_2$, (d) $F_2$, (e) $CF_4$, (f) $CH_4$, (g) $CF_2Cl_2$, (h) $N_2$, (i) $CHF_3$, (j) OCS, (k) $N_2O$, (l) $AsH_3$, (m) $CH_3Cl$, (n) $COCl_2$, (o) $C_2H_2$, (p) $C_2H_4$, (q) $H_2Se$, (r) $H_2S$, (s) $PH_3$, (t) $COF_2$, (u) $CH_3F$, (v) HCHO, (w) $(CH_3)_2O$, and (x) $CH_3NH_2$ adsorbed on $B_{12}N_{12}$. The color code is the same as in Fig. 2.

OCS, and the O atom of the $N_2O$ are bound to the B atom of the $B_{12}N_{12}$ nanocage. Typically, the studied gases are weakly adsorbed on the $B_{12}N_{12}$ nanocage. However, CO, $AsH_3$, $H_2Se$, $H_2S$, $PH_3$, $CH_3F$, HCHO, $(CH_3)_2O$, $NH_3$, and $CH_3NH_2$ are strongly adsorbed on the $B_{12}N_{12}$ nanocage. Typically, the gases strongly interact with the $B_{12}N_{12}$ nanocage at a smaller adsorption distance ($d_{ads}$). Here these $d_{ads}$ values are in the range of 1.61 ($CH_3NH_2$) to 3.12 Å ($Cl_2$) (Table 2). These findings are further validated by the adsorption energy of the gases on the $B_{12}N_{12}$ nanocage (see Table 2) and other structural changes (Table S1, ESI†). In all cases, the adsorption energy of the gases on the $B_{12}N_{12}$ nanocage is negative, suggesting that the adsorption reaction is exothermic in nature. Typically, the gases strongly interact with the $B_{12}N_{12}$ nanocage at higher negative adsorption energies. Here these $E_{ads}$ values are in the range of −0.83 ($H_2$) to −36.84 kcal mol$^{-1}$ ($CH_3NH_2$). The $E_{ads}$ values of the diatomic gases follow the order: $H_2 < F_2 < N_2 < CO < Cl_2 < NO$. The $E_{ads}$ values of the triatomic molecules follow the order: $OCS < CO_2 < N_2O < H_2Se < H_2S$. The $E_{ads}$ value of silane (−2.47 kcal mol$^{-1}$) is higher than that of methane (−1.70 kcal mol$^{-1}$). The $E_{ads}$ values of the hydrocarbon gases follow the order: methane < acetylene < ethylene. The $E_{ads}$ values of the halomethanes follow the order: $CF_4 < CF_2Cl_2 < CHF_3 < CH_3Cl < CH_3F$. The $E_{ads}$ values of

 

Table 3 The reactivity indices, $\mu$, $\eta$, $S$ and $\omega$ for gas-adsorbed $B_{12}N_{12}$ nanocage. The values of $\mu$, $\Delta\mu$, $\eta$, $\Delta\eta$, $\omega$ and $\Delta\omega$ are given in eV; the values of $S$ and $\Delta S$ in $(eV)^{-1}$

| Adsorbate | $\mu$ | $\Delta\mu$ | $\eta$ | $\Delta\eta$ | $S$ | $\Delta S$ | $\omega$ | $\Delta\omega$ |
|---|---|---|---|---|---|---|---|---|
| $SiH_4$ | −4.72 | 0.01 | 4.71 | −0.01 | 0.11 | 0.00 | 2.37 | 0.00 |
| $H_2$ | −4.71 | 0.02 | 4.72 | 0.00 | 0.11 | 0.00 | 2.35 | −0.02 |
| $Cl_2$ | −5.99 | −1.26 | 3.44 | −1.28 | 0.15 | 0.04 | 5.22 | 2.85 |
| $F_2$ | −5.45 | −0.72 | 3.97 | −0.75 | 0.13 | 0.02 | 3.75 | 1.38 |
| $CF_4$ | −4.70 | 0.03 | 4.72 | 0.00 | 0.11 | 0.00 | 2.33 | −0.04 |
| $CH_4$ | −4.71 | 0.02 | 4.72 | 0.00 | 0.11 | 0.00 | 2.34 | −0.03 |
| $CF_2Cl_2$ | −4.66 | 0.07 | 4.72 | 0.00 | 0.11 | 0.00 | 2.31 | −0.06 |
| $N_2$ | −4.67 | 0.06 | 4.72 | 0.00 | 0.11 | 0.00 | 2.31 | −0.06 |
| $CHF_3$ | −4.71 | 0.02 | 4.71 | −0.01 | 0.11 | 0.00 | 2.36 | −0.01 |
| OCS | −4.73 | 0.00 | 4.68 | −0.04 | 0.11 | 0.00 | 2.39 | 0.02 |
| $N_2O$ | −4.70 | 0.03 | 4.71 | −0.01 | 0.11 | 0.00 | 2.35 | −0.02 |
| $AsH_3$ | −4.17 | 0.56 | 4.66 | −0.06 | 0.11 | 0.00 | 1.87 | −0.50 |
| $CH_3Cl$ | −4.62 | 0.11 | 4.71 | −0.01 | 0.11 | 0.00 | 2.27 | −0.10 |
| $COCl_2$ | −5.14 | −0.41 | 4.14 | −0.58 | 0.12 | 0.01 | 3.19 | 0.82 |
| $C_2H_2$ | −4.60 | 0.13 | 4.70 | −0.02 | 0.11 | 0.00 | 2.25 | −0.12 |
| $C_2H_4$ | −4.59 | 0.14 | 4.71 | −0.01 | 0.11 | 0.00 | 2.23 | −0.14 |
| $H_2Se$ | −4.45 | 0.28 | 4.49 | −0.23 | 0.11 | 0.00 | 2.20 | −0.17 |
| $H_2S$ | −4.29 | 0.44 | 4.64 | −0.08 | 0.11 | 0.00 | 1.99 | −0.38 |
| $PH_3$ | −4.10 | 0.63 | 4.66 | −0.06 | 0.11 | 0.00 | 1.80 | −0.57 |
| $COF_2$ | −4.57 | 0.16 | 4.71 | −0.01 | 0.11 | 0.00 | 2.22 | −0.15 |
| $CH_3F$ | −4.46 | 0.27 | 4.71 | −0.01 | 0.11 | 0.00 | 2.11 | −0.26 |
| HCHO | −5.42 | −0.69 | 3.25 | −1.47 | 0.15 | 0.04 | 4.53 | 2.16 |
| $(CH_3)_2O$ | −3.99 | 0.74 | 4.67 | −0.05 | 0.11 | 0.00 | 1.70 | −0.67 |
| $CH_3NH_2$ | −4.00 | 0.73 | 4.57 | −0.15 | 0.11 | 0.00 | 1.75 | −0.62 |

formaldehyde and its halogenated derivatives follow the order: carbonyl fluoride < phosgene < formaldehyde. The $E_{ads}$ value of dimethyl ether (−22.86 kcal $mol^{-1}$) is lower than that of both ammonia (−30.82 kcal $mol^{-1}$) and methylamine. The $E_{ads}$ values of the pnictogen hydrides and methylamine follow the order arsine < phosphine < ammonia < methylamine. As shown in Fig. S3a (ESI†), these adsorption energies are found to be reasonably correlated with the adsorption distances (correlation coefficient of 0.742). Another important observation is that, as shown in Fig. 4a, these adsorption energies are well correlated with the MESP $V_{min\text{-}X}$ values of the gases (correlation coefficient of 0.9468). The angle of the hexagonal ring of the pristine $B_{12}N_{12}$ nanocage is 125°. This angle at the adsorption site decreases by at least 2° due to the adsorption of $AsH_3$, $H_2Se$, $H_2S$, $PH_3$, $CH_3F$, HCHO, $(CH_3)_2O$, and $CH_3NH_2$ (see Table S1, ESI†).

The entropic effects may also influence the adsorption processes. The analysis of $G_{ads}$ values (Table 2) shows that the adsorption of most of the gases on the $B_{12}N_{12}$ nanocage is endergonic, indicative of the weak interactions. However, the adsorption process is found to be exergonic for the HCHO/$B_{12}N_{12}$, $(CH_3)_2O/B_{12}N_{12}$, $NH_3/B_{12}N_{12}$, and $CH_3NH_2/B_{12}N_{12}$ systems. As shown in Fig. S4a (ESI†), these adsorption free energies are also well correlated with the MESP $V_{min\text{-}X}$ values of the gases (correlation coefficient of 0.9041).

The MESP maps of the gas-adsorbed $B_{12}N_{12}$ nanocage are given in Fig. 5. A visual check shows substantial changes in the MESP feature of the isolated molecules, mainly due to the strong gas adsorption. The blue color observed in the $B_{12}N_{12}$ nanocage is more marked in the presence of, for example, formaldehyde, dimethyl ether, and methylamine. The electronic changes associated with the adsorption process could be understood by comparing the MESP $V_{min}$ of the isolated nanocage ($V_{min\text{-}C}$) with that of the gas-adsorbed nanocage (represented as $V_{min\text{-}C'}$) (see, *e.g.*, Fig. S1, ESI†). We find that $\Delta V_{min\text{-}C} = V_{min\text{-}C'} - V_{min\text{-}C}$ is negative for all the studied systems (Table 2). This implies that the $B_{12}N_{12}$ nanocage becomes electron-rich due to the adsorption process. A large magnitude of $\Delta V_{min\text{-}C}$ has been observed, mainly due to the strong gas adsorption. Here these $\Delta V_{min\text{-}C}$ values are in the range of −0.50 ($CH_4/B_{12}N_{12}$ system) to −14.50 kcal $mol^{-1}$ ($CH_3NH_2/B_{12}N_{12}$ system).

The adsorption process could affect the HOMO and LUMO energies (see, *e.g.*, Fig. S5, ESI†), and therefore, the DFT reactivity indices $\mu$, $\eta$, $S$, and $\omega$ (see eqn (2)–(5)). The electrophilicity index $\omega$ consists of both the ability of the system to obtain additional electronic charge (driven by $\mu^2$) and the resistance of the system to exchange electronic charge with the environment (driven by $\eta$). As a result, good electrophiles have higher (lower) values of $\mu(\eta)$. The DFT reactivity indices $\mu$, $\eta$, $S$ and $\omega$ of the $B_{12}N_{12}$ nanocage are −4.73 eV, 4.72 eV, 0.11 $eV^{-1}$ and 2.37 eV, respectively.[27] These DFT reactivity indices for the gas-adsorbed $B_{12}N_{12}$ nanocage are provided in Table 3. Substantial changes are found in these DFT reactivity indices, mainly due to the strong gas adsorption. The change in the reactivity index was calculated by taking the difference between the reactivity index of the gas-adsorbed nanocage and the reactivity index of the corresponding pristine nanocages. For example, the change in $\mu$, $\Delta\mu$, and change in $\eta$, $\Delta\eta$, for the $CH_4/B_{12}N_{12}$ system are 0.02 and 0.00 eV, respectively. The corresponding values for the $CH_3NH_2/B_{12}N_{12}$ system are 0.73 and −0.15 eV respectively.

Table 4 The topological features, $\rho_b$, $\nabla^2\rho_b$, ELF, and LOL for the gas-adsorbed $B_{12}N_{12}$ nanocage. The values are given in a.u

| Adsorbate | $\rho_b$ | $\nabla^2\rho_b$ | ELF | LOL | Adsorbate | $\rho_b$ | $\nabla^2\rho_b$ | ELF | LOL |
|---|---|---|---|---|---|---|---|---|---|
| $SiH_4$ | 0.010 | 0.027 | 0.051 | 0.189 | $CH_3Cl$ | 0.016 | 0.041 | 0.077 | 0.225 |
| $H_2$ | 0.007 | 0.023 | 0.028 | 0.144 | $COCl_2$ | 0.018 | 0.056 | 0.059 | 0.201 |
| $Cl_2$ | 0.005 | 0.019 | 0.015 | 0.109 | $C_2H_2$ | 0.011 | 0.030 | 0.056 | 0.196 |
| $F_2$ | 0.007 | 0.029 | 0.012 | 0.098 | $C_2H_4$ | 0.013 | 0.030 | 0.079 | 0.226 |
| $CF_4$ | 0.012 | 0.041 | 0.032 | 0.153 | $H_2Se$ | 0.049 | −0.002 | 0.529 | 0.515 |
| $CH_4$ | 0.007 | 0.023 | 0.020 | 0.126 | $H_2S$ | 0.064 | −0.030 | 0.516 | 0.508 |
| $CF_2Cl_2$ | 0.012 | 0.043 | 0.033 | 0.155 | $PH_3$ | 0.089 | −0.092 | 0.588 | 0.545 |
| $N_2$ | 0.011 | 0.037 | 0.034 | 0.159 | $COF_2$ | 0.018 | 0.056 | 0.062 | 0.204 |
| $CHF_3$ | 0.009 | 0.037 | 0.018 | 0.119 | $CH_3F$ | 0.031 | 0.080 | 0.104 | 0.254 |
| OCS | 0.008 | 0.027 | 0.030 | 0.150 | HCHO | 0.090 | 0.336 | 0.129 | 0.278 |
| $N_2O$ | 0.016 | 0.048 | 0.054 | 0.193 | $(CH_3)_2O$ | 0.102 | 0.410 | 0.139 | 0.287 |
| $AsH_3$ | 0.067 | −0.053 | 0.683 | 0.595 | $CH_3NH_2$ | 0.125 | 0.314 | 0.219 | 0.346 |

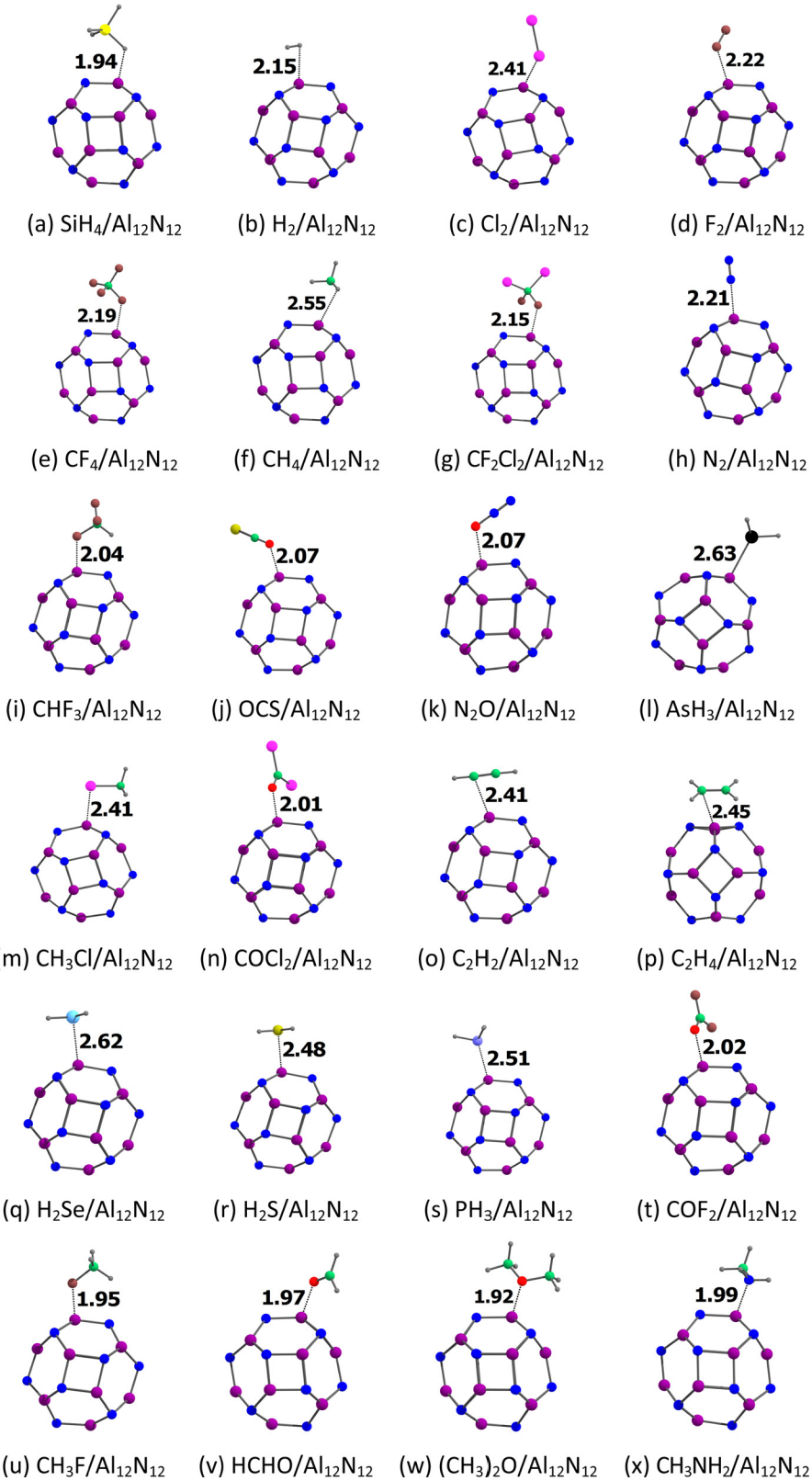


Fig. 6 Optimized structures of gases (a) $SiH_4$, (b) $H_2$, (c) $Cl_2$, (d) $F_2$, (e) $CF_4$, (f) $CH_4$, (g) $CF_2Cl_2$, (h) $N_2$, (i) $CHF_3$, (j) OCS, (k) $N_2O$, (l) $AsH_3$, (m) $CH_3Cl$, (n) $COCl_2$, (o) $C_2H_2$, (p) $C_2H_4$, (q) $H_2Se$, (r) $H_2S$, (s) $PH_3$, (t) $COF_2$, (u) $CH_3F$, (v) HCHO, (w) $(CH_3)_2O$, and (x) $CH_3NH_2$ adsorbed on $Al_{12}N_{12}$. The adsorption distances are given in Å. The color code is the same as in Fig. 3. In addition, the Al atom is denoted by the purple color.

 

Table 5 Adsorption distance, $E_{ads}$, $G_{ads}$, MESP $V_{min}$, and $\Delta V_{min}$ for the gas-adsorbed $Al_{12}N_{12}$ nanocage. $D_{ads}$ is given in Å, other values are given in kcal $mol^{-1}$

| Adsorbate | $d_{ads}$ | $E_{ads}$ | $G_{ads}$ | $V_{min\text{-}C'}$ | $\Delta V_{min\text{-}C}$ |
|---|---|---|---|---|---|
| $SiH_4$ | 1.94 | −7.84 | 1.62 | −57.17 | −8.09 |
| $H_2$ | 2.15 | −3.66 | 3.75 | −55.60 | −6.53 |
| $Cl_2$ | 2.41 | −8.46 | 0.17 | −53.59 | −4.52 |
| $F_2$ | 2.22 | −3.59 | 3.82 | −55.10 | −6.02 |
| $CF_4$ | 2.19 | −4.54 | 5.11 | −56.79 | −7.72 |
| $CH_4$ | 2.55 | −4.65 | 1.52 | −56.16 | −7.09 |
| $CF_2Cl_2$ | 2.15 | −4.94 | 4.89 | −57.92 | −8.85 |
| NO[a] | 2.22 | −9.02 | −0.40 | −56.98 | −7.91 |
| $N_2$ | 2.21 | −6.69 | 1.34 | −57.10 | −8.03 |
| $CHF_3$ | 2.04 | −10.94 | −0.87 | −57.42 | −8.35 |
| OCS | 2.07 | −9.50 | −0.53 | −60.37 | −11.30 |
| $CO_2$[a] | 2.08 | −11.17 | −2.52 | −57.86 | −8.79 |
| $N_2O$ | 2.07 | −12.93 | −3.81 | −59.11 | −10.04 |
| CO[a] | 2.20 | −11.68 | −3.04 | −57.23 | −8.16 |
| $AsH_3$ | 2.63 | −14.12 | −4.29 | −60.05 | −10.98 |
| $CH_3Cl$ | 2.41 | −15.12 | −4.48 | −59.49 | −10.42 |
| $COCl_2$ | 2.01 | −14.90 | −3.94 | −62.00 | −12.93 |
| $C_2H_2$ | 2.41 | −14.35 | −7.61 | −58.17 | −9.10 |
| $C_2H_4$ | 2.45 | −14.93 | −4.51 | −58.61 | −9.54 |
| $H_2Se$ | 2.62 | −15.80 | −6.29 | −59.36 | −10.29 |
| $H_2S$ | 2.48 | −16.74 | −7.26 | −59.30 | −10.23 |
| $PH_3$ | 2.51 | −17.54 | −8.03 | −60.30 | −11.23 |
| $COF_2$ | 2.02 | −14.81 | −4.39 | −60.74 | −11.67 |
| $CH_3F$ | 1.95 | −17.72 | −7.49 | −60.74 | −11.67 |
| HCHO | 1.97 | −26.09 | −14.15 | −62.94 | −13.87 |
| $(CH_3)_2O$ | 1.92 | −33.18 | −21.28 | −61.43 | −12.36 |
| $NH_3$[a] | 2.01 | −36.83 | −26.53 | −62.12 | −13.05 |
| $CH_3NH_2$ | 1.99 | −40.19 | −28.68 | −61.43 | −12.36 |

[a] Taken from ref. 27.

The results of the QTAIM analysis of the gas-adsorbed $B_{12}N_{12}$ nanocage are provided in Fig. S6 (ESI†) and Table 4. For the $AsH_3/B_{12}N_{12}$, $H_2Se/B_{12}N_{12}$, $H_2S/B_{12}N_{12}$, and $PH_3/B_{12}N_{12}$ systems, $\rho_b$ values are in the range of 0.0491 ($H_2Se/B_{12}N_{12}$ system) to 0.0888 a.u. ($PH_3/B_{12}N_{12}$ system) and the corresponding $\nabla^2\rho_b$ values are negative. The QTAIM analysis suggests the covalent nature of interactions in these systems. For the rest of the systems, $\rho_b$ values are in the range of 0.0051 ($Cl_2/B_{12}N_{12}$ system) to 0.1252 a.u. ($CH_3NH_2/B_{12}N_{12}$ system) and the corresponding $\nabla^2\rho_b$ values are positive. The QTAIM analysis suggests the noncovalent nature of interactions in these systems. For all the systems, the values of ELF and LOL are in the ranges of 0.012–0.683 and 0.098–0.595 a.u., respectively (see Table 4). The values of ELF $>$ 0.5 and LOL $>$ 0.5 in the $AsH_3/B_{12}N_{12}$, $H_2Se/B_{12}N_{12}$, $H_2S/B_{12}N_{12}$, and $PH_3/B_{12}N_{12}$ systems are also indicative of covalent interactions.

The NCI analysis provides the reduced density gradient (RDG) isosurface and the plots of the RDG *versus* sign($\lambda_2$)$\rho$, where $\lambda_2$ is the second eigenvalue of the electron density Hessian matrix. The results of the NCI analysis of the gas-adsorbed $B_{12}N_{12}$ nanocage are provided in Fig. S7a and S8 (ESI†). The H-bond, van der Waals, and steric interactions can be visualized by blue, green, and red colors, respectively, in the NCI isosurface. Also, the H-bond (sign($\lambda_2$)$\rho$ $<$ 0), van der Waals (sign($\lambda_2$)$\rho$ $\approx$ 0), and steric (sign($\lambda_2$)$\rho$ $>$ 0) interactions can be visualized as blue, green, and red colored spikes, respectively, in the RDG graph. The NCI results indicate the presence of van der Waals interactions between the gas molecules and the $B_{12}N_{12}$ nanocage, except for the $AsH_3/B_{12}N_{12}$, $H_2Se/B_{12}N_{12}$, $H_2S/B_{12}N_{12}$, and $PH_3/B_{12}N_{12}$ systems. Overall, the steric interactions between the gas molecules and the $B_{12}N_{12}$ nanocage increases as the size of the gas molecules increases.

### 3.3. Adsorption of gases on $Al_{12}N_{12}$

The optimized structures of the gases adsorbed on the $Al_{12}N_{12}$ nanocage are given in Fig. 6. The studied gases are preferably bound to the Al atom rather than the N atom of the $Al_{12}N_{12}$ nanocage. Notably, the F atom of the $CF_2Cl_2$, the O atom of the OCS, and the O atom of the $N_2O$ are bound to the Al atom of the $Al_{12}N_{12}$ nanocage. Typically, the studied gases are strongly adsorbed on the $Al_{12}N_{12}$ nanocage. However, $H_2$, $F_2$, $CF_4$, $CH_4$, $CF_2Cl_2$, and NO are weakly adsorbed on the $Al_{12}N_{12}$ nanocage. Typically, the gases strongly interact with the $Al_{12}N_{12}$ nanocage at a smaller adsorption distance ($d_{ads}$). Here these $d_{ads}$ values are in the range of 1.92 ($(CH_3)_2O$) to 2.63 Å ($AsH_3$) (Table 5). These findings are further validated by the adsorption energy of the gases on the $Al_{12}N_{12}$ nanocage (see Table 5) and other structure changes (Table S2, ESI†). In all cases, the adsorption energy of the gases on the $Al_{12}N_{12}$ nanocage is negative, suggesting that the adsorption reaction is exothermic in nature. Typically, the gases strongly interact with the $Al_{12}N_{12}$ nanocage at higher negative adsorption energies. Here these $E_{ads}$ values are in the range of −3.59 ($F_2$) to −40.19 kcal $mol^{-1}$ ($CH_3NH_2$). The $E_{ads}$ values of the diatomic gases follow the order: $F_2$ $<$ $H_2$ $<$ $N_2$ $<$ $Cl_2$ $<$ NO $<$ CO. The $E_{ads}$ values of the triatomic molecules follow the order: OCS $<$ $CO_2$ $<$ $N_2O$ $<$ $H_2Se$ $<$ $H_2S$. The $E_{ads}$ value of silane (−7.84 kcal $mol^{-1}$) is higher than that of methane (−4.65 kcal $mol^{-1}$). The $E_{ads}$ values of the hydrocarbon gases follow the order: methane $<$ acetylene $<$ ethylene. The $E_{ads}$ values of the halomethanes follow the order: $CF_4$ $<$ $CF_2Cl_2$ $<$ $CHF_3$ $<$ $CH_3Cl$ $<$ $CH_3F$. The $E_{ads}$ values of formaldehyde and its halogenated derivatives follow the order: carbonyl fluoride $<$ phosgene $<$ formaldehyde. The $E_{ads}$ value of dimethyl ether (−33.18 kcal $mol^{-1}$) is lower than that of both ammonia (−36.83 kcal $mol^{-1}$) and methylamine. The $E_{ads}$ values of the pnictogen hydrides and methylamine follow the order arsine $<$ phosphine $<$ ammonia $<$ methylamine. As shown in Fig. S3b (ESI†), these adsorption energies are not well correlated with the adsorption distances (correlation coefficient of 0.293). Another important observation is that, as shown in Fig. 4b, these adsorption energies are well correlated with the MESP $V_{min\text{-}X}$ values of the gases (correlation coefficient of 0.9808). The angle of the hexagonal ring of the pristine $Al_{12}N_{12}$ nanocage is 125°. This angle at the adsorption site is almost unaffected by the adsorption of $H_2$, $F_2$, $CF_4$, $CH_4$, and $CF_2Cl_2$ (see Table S2, ESI†).

The analysis of $G_{ads}$ values (Table 5) shows that the adsorption of most of the gases on the $Al_{12}N_{12}$ nanocage is exergonic, indicative of the stronger interactions. However, the adsorption process is found to be endergonic for the $SiH_4/Al_{12}N_{12}$, $H_2/Al_{12}N_{12}$, $Cl_2/Al_{12}N_{12}$, $F_2/Al_{12}N_{12}$, $CF_4/Al_{12}N_{12}$, $CH_4/Al_{12}N_{12}$ $CF_2Cl_2/Al_{12}N_{12}$, and $N_2/Al_{12}N_{12}$ systems. As shown in Fig. S4b (ESI†), these adsorption free energies are also well correlated

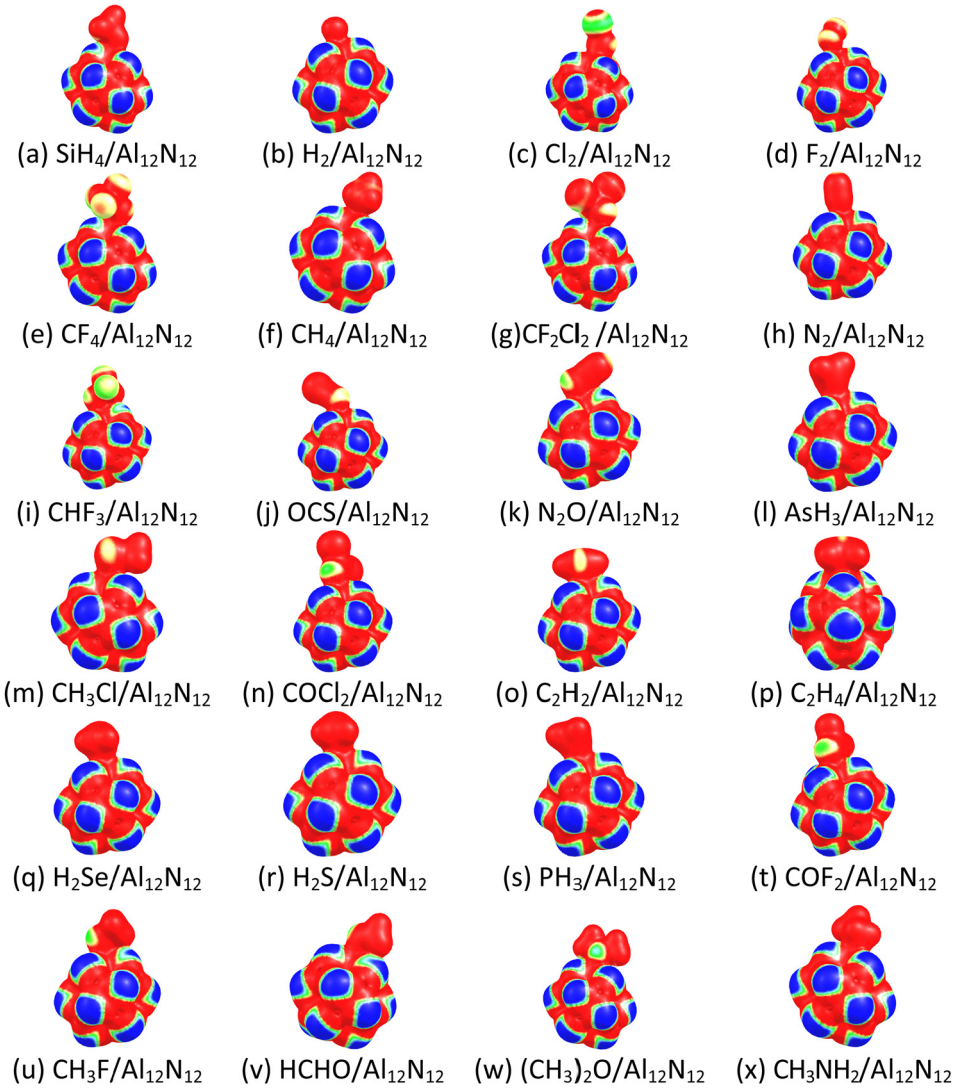


Fig. 7 MESP mapped onto 0.01 a.u. electron density isosurface of gases (a) $SiH_4$, (b) $H_2$, (c) $Cl_2$, (d) $F_2$, ® $CF_4$, (f) $CH_4$, (g) $CF_2Cl_2$, (h) $N_2$, (i) $CHF_3$, (j) OCS, (k) $N_2O$, (l) $AsH_3$, (m) $CH_3Cl$, (n) $COCl_2$, (o) $C_2H_2$, (p) $C_2H_4$, (q) $H_2S$®(r) $H_2S$, (s) $PH_3$, (t) $COF_2$, (u) $CH_3F$, (v) HCHO, (w) $(CH_3)_2O$, and (x) $CH_3NH_2$ adsorbed on $Al_{12}N_{12}$. The color code is the same as in Fig. 2.

with the MESP $V_{min\text{-}X}$ values of the gases (correlation coefficient of 0.9818).

The MESP maps of the gas-adsorbed $Al_{12}N_{12}$ nanocage are given in Fig. 7. A visual check shows substantial changes in the MESP feature of most of the isolated gas molecules due to the adsorption process. The blue region (most electron-rich region) in, for example, the formaldehyde, dimethyl ether, and methylamine molecules is less marked in the presence of $Al_{12}N_{12}$. We find that $\Delta V_{min\text{-}C}$ is negative for all the studied systems (Table 5). This implies that the $Al_{12}N_{12}$ nanocage becomes electron-rich due to the adsorption process. Here in most of the systems, a large magnitude of $\Delta V_{min\text{-}C}$ has been observed due to the adsorption process. These $\Delta V_{min\text{-}C}$ values are in the range of −4.52 ($Cl_2/Al_{12}N_{12}$ system) to −13.87 kcal $mol^{-1}$ (HCHO/$Al_{12}N_{12}$ system).

The DFT reactivity indices $\mu$, $\eta$, $S$ and $\omega$ of the $Al_{12}N_{12}$ nanocage are −4.86 eV, 3.16 eV, 0.16 $eV^{-1}$ and 3.74 eV, respectively.[27] In most of the systems, substantial changes are observed in these DFT reactivity indices due to the adsorption process (Table 6). For example, $\Delta\mu$ and $\Delta\eta$ for the $CH_4/Al_{12}N_{12}$ system are 0.11 and 0.00 eV, respectively. The corresponding values for the $CH_3NH_2/Al_{12}N_{12}$ system are 0.43 and −0.03 eV respectively.

The results of the QTAIM analysis of the gas-adsorbed $Al_{12}N_{12}$ nanocage are provided in Fig. S9 (ESI†) and Table 7. For all the systems, $\rho_b$ values are in the range of 0.0122 ($CH_4/Al_{12}N_{12}$ system) to 0.0587 a.u. ($CH_3NH_2/Al_{12}N_{12}$ system) and the corresponding $\nabla^2\rho_b$ values are positive. For all the systems, the values of ELF and LOL are in the ranges of 0.030–0.214 and 0.150–0.343 a.u., respectively (see Table 7). These results suggest the noncovalent nature of interactions in these systems. The results of the NCI analysis of the gas-adsorbed $Al_{12}N_{12}$ nanocage are provided in Fig. S7b and S10 (ESI†). The NCI results indicate the presence of van der Waals interactions

 

Table 6 The reactivity indices, $\mu$, $\eta$, $S$ and $\omega$ for the gas-adsorbed $Al_{12}N_{12}$ nanocage. The values of $\mu$, $\Delta\mu$, $\eta$, $\Delta\eta$, $\omega$ and $\Delta\omega$ are given in eV; the values of $S$ and $\Delta S$ in $(eV)^{-1}$

| Adsorbate | $\mu$ | $\Delta\mu$ | $\eta$ | $\Delta\eta$ | $S$ | $\Delta S$ | $\omega$ | $\Delta\omega$ |
|---|---|---|---|---|---|---|---|---|
| $SiH_4$ | −4.69 | 0.17 | 3.16 | 0.00 | 0.16 | 0.00 | 3.49 | −0.25 |
| $H_2$ | −4.75 | 0.11 | 3.18 | 0.02 | 0.16 | 0.00 | 3.54 | −0.20 |
| $Cl_2$ | −5.32 | −0.46 | 2.80 | −0.36 | 0.18 | 0.02 | 5.06 | 1.32 |
| $F_2$ | −5.44 | −0.58 | 2.52 | −0.64 | 0.20 | 0.04 | 5.87 | 2.13 |
| $CF_4$ | −4.71 | 0.15 | 3.18 | 0.02 | 0.16 | 0.00 | 3.50 | −0.24 |
| $CH_4$ | −4.75 | 0.11 | 3.16 | 0.00 | 0.16 | 0.00 | 3.57 | −0.17 |
| $CF_2Cl_2$ | −4.66 | 0.20 | 3.17 | 0.01 | 0.16 | 0.00 | 3.43 | −0.31 |
| $N_2$ | −4.68 | 0.18 | 3.19 | 0.03 | 0.16 | 0.00 | 3.44 | −0.30 |
| $CHF_3$ | −4.71 | 0.15 | 3.16 | 0.00 | 0.16 | 0.00 | 3.52 | −0.22 |
| OCS | −4.59 | 0.27 | 3.15 | −0.01 | 0.16 | 0.00 | 3.33 | −0.41 |
| $N_2O$ | −4.63 | 0.23 | 3.15 | −0.01 | 0.16 | 0.00 | 3.40 | −0.34 |
| $AsH_3$ | −4.52 | 0.34 | 3.16 | 0.00 | 0.16 | 0.00 | 3.24 | −0.50 |
| $CH_3Cl$ | −4.60 | 0.26 | 3.16 | 0.00 | 0.16 | 0.00 | 3.34 | −0.40 |
| $COCl_2$ | −4.93 | −0.07 | 2.74 | −0.42 | 0.18 | 0.02 | 4.43 | 0.69 |
| $C_2H_2$ | −4.59 | 0.27 | 3.16 | 0.00 | 0.16 | 0.00 | 3.33 | −0.41 |
| $C_2H_4$ | −4.60 | 0.26 | 3.15 | −0.01 | 0.16 | 0.00 | 3.35 | −0.39 |
| $H_2Se$ | −4.56 | 0.30 | 3.16 | 0.00 | 0.16 | 0.00 | 3.29 | −0.45 |
| $H_2S$ | −4.58 | 0.28 | 3.16 | 0.00 | 0.16 | 0.00 | 3.32 | −0.42 |
| $PH_3$ | −4.51 | 0.35 | 3.16 | 0.00 | 0.16 | 0.00 | 3.21 | −0.53 |
| $COF_2$ | −4.56 | 0.30 | 3.17 | 0.01 | 0.16 | 0.00 | 3.29 | −0.45 |
| $CH_3F$ | −4.53 | 0.33 | 3.14 | −0.02 | 0.16 | 0.00 | 3.27 | −0.47 |
| HCHO | −4.75 | 0.11 | 2.87 | −0.29 | 0.17 | 0.01 | 3.93 | 0.19 |
| $(CH_3)_2O$ | −4.45 | 0.41 | 3.14 | −0.02 | 0.16 | 0.00 | 3.16 | −0.58 |
| $CH_3NH_2$ | −4.43 | 0.43 | 3.13 | −0.03 | 0.16 | 0.00 | 3.13 | −0.61 |

between the gas molecules and the $Al_{12}N_{12}$ nanocage. Overall, the steric interactions between the gas molecules and the $Al_{12}N_{12}$ nanocage increase as the size of the gas molecules increases.

Our results show that only $AsH_3$, $H_2Se$, $H_2S$, $PH_3$, $CH_3F$, HCHO, $(CH_3)_2O$, and $CH_3NH_2$ are strongly adsorbed on the $B_{12}N_{12}$ nanocage. Furthermore, only $H_2$, $F_2$, $CF_4$, $CH_4$, and $CF_2Cl_2$ are weakly adsorbed on the $Al_{12}N_{12}$ nanocage. Overall, our results indicate that the $Al_{12}N_{12}$ nanoclusters may have a higher potential in gas storage and catalytic applications than the $B_{12}N_{12}$ nanoclusters. The stronger the adsorption of gas molecules, the more difficult it is for them to desorb from the surface.[78] The gas-sensing behavior of the $Al_{12}N_{12}$ nanocage might have a severe influence on the reusability of gas sensors. The MESP of a molecule is a real physical property that can be determined experimentally by X-ray diffraction techniques or by computational methods.[58] There is a strong linear correlation between the adsorption energies of the gas-adsorbed $B_{12}N_{12}$ and $Al_{12}N_{12}$ systems and the MESP $V_{min}$ values of the gases (see Fig. 4). This enables us to predict the adsorption energies once we know the MESP features of the gas molecules.

# 4. Conclusions

The adsorption of twenty-four gases ($SiH_4$, $H_2$, $Cl_2$, $F_2$, $CF_4$, $CH_4$, $CF_2Cl_2$, $N_2$, $CHF_3$, OCS, $N_2O$, $AsH_3$, $CH_3Cl$, $COCl_2$, $C_2H_2$, $C_2H_4$, $H_2Se$, $H_2S$, $PH_3$, $COF_2$, $CH_3F$, HCHO, $(CH_3)_2O$, and $CH_3NH_2$) on the $B_{12}N_{12}$ and $Al_{12}N_{12}$ nanocages was studied using DFT calculations. Most of the studied gases are weakly adsorbed on the $B_{12}N_{12}$ nanocage. However, $AsH_3$, $H_2Se$, $H_2S$, $PH_3$, $CH_3F$, HCHO, $(CH_3)_2O$, and $CH_3NH_2$ are strongly adsorbed on the $B_{12}N_{12}$ nanocage. The gases strongly interact with the nanocage usually at a smaller adsorption distance and a higher negative adsorption energy. For the gas-adsorbed $B_{12}N_{12}$ system, the $d_{ads}$ values are in the range of 1.61 ($CH_3NH_2$) to 3.12 Å ($Cl_2$), and the $E_{ads}$ values are in the range of −0.83 ($H_2$) to −36.84 kcal $mol^{-1}$ ($CH_3NH_2$). Here the adsorption energies are found to be reasonably correlated with the adsorption distances. Another important observation is that these adsorption energies are well correlated with the MESP $V_{min}$ values of the gases. Substantial changes are found in the DFT reactivity indices ($\mu$, $\eta$, $S$ and $\omega$) of the $B_{12}N_{12}$ nanocage, mainly due to the strong gas adsorption. For example, $\Delta\mu$ and $\Delta\eta$ for the $CH_4/B_{12}N_{12}$ system are 0.02 and 0.00 eV, respectively. The corresponding values for the $CH_3NH_2/B_{12}N_{12}$ system are 0.73 and −0.15 eV respectively. The QTAIM analysis suggests the covalent nature of interactions in the $AsH_3/B_{12}N_{12}$, $H_2Se/B_{12}N_{12}$, $H_2S/B_{12}N_{12}$, and $PH_3/B_{12}N_{12}$ systems.

Most of the studied gases are strongly adsorbed on the $Al_{12}N_{12}$ nanocage. However, $H_2$, $F_2$, $CF_4$, $CH_4$, and $CF_2Cl_2$ are weakly adsorbed on the $Al_{12}N_{12}$ nanocage. For the gas-adsorbed $Al_{12}N_{12}$ system, the $d_{ads}$ values are in the range of 1.92 ($(CH_3)_2O$) to 2.63 Å ($AsH_3$), and the $E_{ads}$ values are in the range of −3.59 ($F_2$) to −40.19 kcal $mol^{-1}$ ($CH_3NH_2$). These adsorption energies are also well correlated with the MESP $V_{min\text{-}X}$ values of the gases. In most of the systems, substantial changes are observed in the DFT reactivity indices ($\mu$, $\eta$, $S$ and $\omega$) of the $Al_{12}N_{12}$ nanocage due to the gas adsorption. For example, $\Delta\mu$ and $\Delta\eta$ for the $CH_4/Al_{12}N_{12}$ system are 0.11 and 0.00 eV, respectively. The corresponding values for the $CH_3NH_2/Al_{12}N_{12}$ system are 0.43 and −0.03 eV

Table 7 The topological features, $\rho_b$, $\nabla^2\rho_b$, ELF, and LOL for the gas-adsorbed $Al_{12}N_{12}$ nanocage. The values are given in a.u

| Adsorbate | $\rho_b$ | $\nabla^2\rho_b$ | ELF | LOL | Adsorbate | $\rho_b$ | $\nabla^2\rho_b$ | ELF | LOL |
|---|---|---|---|---|---|---|---|---|---|
| $SiH_4$ | 0.028 | 0.082 | 0.085 | 0.234 | $CH_3Cl$ | 0.040 | 0.165 | 0.081 | 0.229 |
| $H_2$ | 0.020 | 0.063 | 0.058 | 0.198 | $COCl_2$ | 0.042 | 0.276 | 0.048 | 0.184 |
| $Cl_2$ | 0.048 | 0.134 | 0.214 | 0.343 | $C_2H_2$ | 0.029 | 0.085 | 0.093 | 0.243 |
| $F_2$ | 0.021 | 0.100 | 0.034 | 0.157 | $C_2H_4$ | 0.029 | 0.069 | 0.116 | 0.266 |
| $CF_4$ | 0.022 | 0.118 | 0.030 | 0.150 | $H_2Se$ | 0.032 | 0.082 | 0.111 | 0.261 |
| $CH_4$ | 0.012 | 0.034 | 0.068 | 0.213 | $H_2S$ | 0.035 | 0.103 | 0.104 | 0.254 |
| $CF_2Cl_2$ | 0.024 | 0.137 | 0.030 | 0.151 | $PH_3$ | 0.038 | 0.096 | 0.125 | 0.275 |
| $N_2$ | 0.028 | 0.148 | 0.042 | 0.173 | $COF_2$ | 0.040 | 0.258 | 0.048 | 0.184 |
| $CHF_3$ | 0.032 | 0.208 | 0.037 | 0.164 | $CH_3F$ | 0.041 | 0.294 | 0.042 | 0.173 |
| OCS | 0.034 | 0.208 | 0.095 | 0.245 | HCHO | 0.049 | 0.325 | 0.059 | 0.200 |
| $N_2O$ | 0.036 | 0.212 | 0.047 | 0.183 | $(CH_3)_2O$ | 0.056 | 0.395 | 0.060 | 0.201 |
| $AsH_3$ | 0.033 | 0.072 | 0.128 | 0.277 | $CH_3NH_2$ | 0.059 | 0.335 | 0.082 | 0.230 |

respectively. The QTAIM analysis suggests the noncovalent nature of interactions in the gas-adsorbed $Al_{12}N_{12}$ systems.

## Conflicts of interest

There are no conflicts to declare.

## Acknowledgements

This publication is based upon work supported by the King Abdullah University of Science and Technology (KAUST) Office of Sponsored Research (OSR) under award no. ORFS-2022-CRG11-5028. R. G. S. N. and A. K. N. N. would like to thank KAUST for providing the computational resources of the Shaheen II supercomputer.

## References

1 U.S. EPA's report global mitigation of non-$CO_2$ greenhouse gases: 2010–2030.
2 H. Tian, *et al.*, *Nature*, 2020, **586**, 248–256.
3 J. F. d S. Petruci and A. A. Cardoso, *Anal. Chem.*, 2016, **88**, 11714–11719.
4 P. D. N. Svoronos and T. J. Bruno, *Ind. Eng. Chem. Res.*, 2002, **41**, 5321–5336.
5 G. W. Gribble, *J. Nat. Prod.*, 1992, **55**, 1353–1395.
6 F. S. Rowland, *Am. Sci.*, 1989, **77**, 36–45.
7 J.-R. Chen, H.-Y. Tsai, S.-K. Chen, H.-R. Pan, S.-C. Hu, C.-C. Shen, C.-M. Kuan, Y.-C. Lee and C.-C. Wu, *Proc. Safety Prog.*, 2006, **25**, 237–244.
8 Y. N. Ko, S. H. Choi and Y. C. Kang, *ACS Appl. Mater. Interfaces*, 2016, **8**, 6449–6456.
9 C. Winder, *Environ. Res.*, 2001, **85**, 105–114.
10 J. Wang, M. Sánchez-Roselló, J. L. Aceña, C. del Pozo, A. E. Sorochinsky, S. Fustero, V. A. Soloshonok and H. Liu, *Chem. Rev.*, 2014, **114**, 2432–2506.
11 D. L. Sudakin, *Hum. Exp. Toxicol.*, 2005, **24**, 27–33.
12 D. Pakulska and S. Czerczak, *Int. J. Occup. Med. Environ. Health*, 2006, **19**, 36–44.
13 J. Borak and W. F. Diller, *J. Occup. Environ. Med.*, 2001, **43**, 110–119.
14 Y. Mitsui, Y. Ohira, T. Yonemura, T. Takaichi, A. Sekiya and T. Beppu, *J. Electrochem. Soc.*, 2004, **151**, G297.
15 T. Salthammer, S. Mentese and R. Marutzky, *Chem. Rev.*, 2010, **110**, 2536–2572.
16 T. H. Fleisch, A. Basu, M. J. Gradassi and J. G. Masin, *Stud. Surf. Sci. Catal.*, 1997, **107**, 117–125.
17 S. R. Raga, Y. Jiang, L. K. Ono and Y. Qi, *Energy Technol.*, 2017, **5**, 1750–1761.
18 D. Mori and K. Hirose, *Int. J. Hydrogen Energy*, 2009, **34**, 4569–4574.
19 C. Nguyen and D. D. Do, *Langmuir*, 1999, **15**, 3608–3615.
20 V. K. Gupta and T. A. Saleh, *Environ. Sci. Pollut. Res. Int.*, 2013, **20**, 2828–2843.
21 S. Gadipelli and Z. X. Guo, *Prog. Mater. Sci.*, 2015, **69**, 1–60.
22 N. Rangnekar, N. Mittal, B. Elyassi, J. Caro and M. Tsapatsis, *Chem. Soc. Rev.*, 2015, **44**, 7128–7154.
23 Y. Yang, A. K. Narayanan Nair and S. Sun, *J. Phys. Chem. C*, 2020, **124**, 16478–16487.
24 Y. Yang, A. K. Narayanan Nair and S. Sun, *Ind. Eng. Chem. Res.*, 2021, **60**, 7729–7738.
25 A. K. Narayanan Nair, R. Cui and S. Sun, *ACS Earth Space Chem.*, 2021, **5**, 2599–2611.
26 R. Geetha Sadasivan Nair, A. Kumar Narayanan Nair and S. Sun, *J. Mol. Liq.*, 2023, 122923.
27 R. Geetha Sadasivan Nair, A. K. Narayanan Nair and S. Sun, *Energy Fuels*, 2023, **37**, 14053–14063.
28 A. Abbasi and J. Jahanbin Sardroodi, *Environ. Sci.: Nano*, 2016, **3**, 1153–1164.
29 A. Abbasi, J. J. Sardroodi and A. R. Ebrahimzadeh, *Surf. Sci.*, 2016, **654**, 20–32.
30 A. Abbasi and J. J. Sardroodi, *Surf. Interfaces*, 2017, **8**, 15–27.
31 A. Abbasi and J. Jahanbin Sardroodi, *New J. Chem.*, 2017, **41**, 12569–12580.
32 A. Abbasi and J. J. Sardroodi, *J. Nanostruct. Chem.*, 2017, **7**, 345–358.
33 C. Zhao and H. Wu, *Appl. Surf. Sci.*, 2018, **435**, 1199–1212.
34 A. Abbasi and J. J. Sardroodi, *Comput. Theor. Chem.*, 2018, **1125**, 15–28.
35 A. Abbasi and J. J. Sardroodi, *Phys. E*, 2019, **108**, 382–390.
36 A. Abbasi and J. J. Sardroodi, *Appl. Surf. Sci.*, 2019, **469**, 781–791.
37 A. Abbasi, A. Abdelrasoul and J. J. Sardroodi, *Adsorption*, 2019, **25**, 1001–1017.
38 J. Beheshtian, A. A. Peyghan, Z. Bagheri and M. Kamfiroozi, *Struct. Chem.*, 2012, **23**, 1567–1572.
39 K. Kalateh and A. Abdolmanafi, *Int. J. New Chem.*, 2015, **2**, 1–7.
40 E. Shakerzadeh, *Phys. E*, 2016, **78**, 1–9.
41 A. Bahrami, M. B. Qarai and N. L. Hadipour, *Comput. Theor. Chem.*, 2017, **1108**, 63–69.
42 A. S. Rad, *Semiconductors*, 2017, **51**, 134–138.
43 S. Larki, E. Shakerzadeh, E. C. Anota and R. Behjatmanesh-Ardakani, *Chem. Phys.*, 2019, **526**, 110424.
44 A. Shokuhi Rad, D. Zareyee, V. Pouralijan Foukolaei, B. Kamyab Moghadas and M. Peyravi, *Mol. Phys.*, 2016, **114**, 3143–3149.
45 L. Saedi, Z. Javanshir, S. Khanahmadzadeh, M. Maskanati and M. Nouraliei, *Mol. Phys.*, 2020, **118**, e1658909.
46 A. S. Rad and K. Ayub, *Mater. Chem. Phys.*, 2017, **194**, 337–344.
47 M. Y. Mehboob, R. Hussain, F. Younas, S. Jamil, M. M. A. Iqbal, K. Ayub, N. Sultana and M. R. S. A. Janjua, *J. Clust. Sci.*, 2023, **34**, 1237–1247.
48 A. S. Rad and K. Ayub, *Vacuum*, 2016, **133**, 70–80.
49 Q. Wang, Q. Sun, P. Jena and Y. Kawazoe, *ACS Nano*, 2009, **3**, 621–626.
50 A. S. Rad, *J. Theory Comput. Chem.*, 2018, **17**, 1850013.
51 R. Padash, M. Rahimi-Nasrabadi, A. Shokuhi Rad, A. Sobhani-Nasab, T. Jesionowski and H. Ehrlich, *J. Clust. Sci.*, 2019, **30**, 203–218.



 

52 T. Oku, A. Nishiwaki and I. Narita, *Sci. Technol. Adv.*, 2004, **5**, 635–638.
53 C. Balasubramanian, S. Bellucci, P. Castrucci, M. De Crescenzi and S. V. Bhoraskar, *Chem. Phys. Lett.*, 2004, **383**, 188–191.
54 C. Liu, Z. Hu, Q. Wu, X. Wang, Y. Chen, H. Sang, J. Zhu, S. Deng and N. Xu, *J. Am. Chem. Soc.*, 2005, **127**, 1318–1322.
55 H.-S. Wu, F.-Q. Zhang, X.-H. Xu, C.-J. Zhang and H. Jiao, *J. Phys. Chem. A*, 2003, **107**, 204–209.
56 G. S. Remya and C. H. Suresh, *New J. Chem.*, 2018, **42**, 3602–3608.
57 G. S. Remya and C. H. Suresh, *New J. Chem.*, 2019, **43**, 14634–14642.
58 C. H. Suresh, G. S. Remya and P. K. Anjalikrishna, *Wiley Interdiscip. Rev.: Comput. Mol. Sci.*, 2022, **12**, e1601.
59 M. J. Frisch, *et al.*, *Gaussian 16, Revision A.03*, Gaussian, Inc., Wallingford, CT, 2016.
60 Y. Zhao and D. G. Truhlar, *Theor. Chem. Acc.*, 2008, **120**, 215–241.
61 H. Chermette, *J. Comput. Chem.*, 1999, **20**, 129–154.
62 R. G. Parr, R. A. Donnelly, M. Levy and W. E. Palke, *J. Chem. Phys.*, 1978, **68**, 3801–3807.
63 L. R. Domingo, M. Ríos-Gutiérrez and P. Pérez, *Molecules*, 2016, **21**, 748.
64 P. K. Chattaraj, U. Sarkar and D. R. Roy, *Chem. Rev.*, 2006, **106**, 2065–2091.
65 R. G. Parr and R. G. Pearson, *J. Am. Chem. Soc.*, 1983, **105**, 7512–7516.
66 R. G. Parr, L. v Szentpály and S. Liu, *J. Am. Chem. Soc.*, 1999, **121**, 1922–1924.
67 S. F. Boys and F. Bernardi, *Mol. Phys.*, 1970, **19**, 553–566.
68 R. F. Bader, *Chem. Rev.*, 1991, **91**, 893–928.
69 T. Lu and F. Chen, *J. Comput. Chem.*, 2012, **33**, 580–592.
70 P. A. Hunt, C. R. Ashworth and R. P. Matthews, *Chem. Soc. Rev.*, 2015, **44**, 1257–1288.
71 S. Khan, H. Sajid, K. Ayub and T. Mahmood, *J. Mol. Liq.*, 2020, **316**, 113860.
72 A. Savin, R. Nesper, S. Wengert and T. F. Fässler, *Angew. Chem., Int. Ed. Engl.*, 1997, **36**, 1808–1832.
73 A. V. Afonin, V. A. Semenov and A. V. Vashchenko, *Phys. Chem. Chem. Phys.*, 2021, **23**, 24536–24540.
74 E. R. Johnson, S. Keinan, P. Mori-Sánchez, J. Contreras-García, A. J. Cohen and W. Yang, *J. Am. Chem. Soc.*, 2010, **132**, 6498–6506.
75 J. Contreras-García, E. R. Johnson, S. Keinan, R. Chaudret, J. P. Piquemal, D. N. Beratan and W. Yang, *J. Chem. Theory Comput.*, 2011, **7**, 625–632.
76 T. Williams and C. Kelley, *GNUplot: an interactive plotting program*, 1998.
77 W. Humphrey, A. Dalke and K. Schulten, *J. Mol. Graph.*, 1996, **14**, 33–38.
78 A. L. Pereira Silva and J. d J. G. Varela Júnior, *Inorg. Chem.*, 2023, **62**, 1926–1934.